Analysis and Design Optimization of Axial - Radial Flux Hybrid Excitation Permanent Magnet Eddy Current Coupling

Hongming Zhang *, Chengcheng Liu †, Shiwei Zhang **, Youhua Wang *, Gang Lei ****, and Jianguo Zhu *******

Abstract – This paper proposes an axial - radial flux hybrid excitation permanent magnet eddy current coupling (HE-PMEC), where the ferrite magnet is employed for producing the radial flux and the DC excitation current is adopted for producing the axial flux. Moreover, a shielding layer is developed to regulate the radial magnetic field. Its magnetic field distribution, electromagnetic performance, and temperature distribution are calculated based on the 3D finite element method (FEM). By adjusting the applied DC excitation current density and the insertion depth of the shielding layer, the variable current starting process, the variable current braking process, and the speed regulation characteristic of the proposed HE-PMEC are obtained. It can be seen that the starting process, braking process, and speed regulation ability of the HE-PMEC have been enhanced greatly. Furthermore, the copper ring shape of the HE-PMEC is optimized by using the proposed improved multilevel optimization method. It can be seen that the performance of the HE-PMEC can be improved by using the new optimized copper ring shape. Lastly, compared with the conventional PMECs, the proposed HE-PMEC has shown its superior electromagnetic performance.

Keywords: Hybrid excitation, Permanent magnet eddy current coupling (PMEC), Electromagnetic-temperature field, Improved multilevel optimization

1. Introduction

Traditional gears or couplings require a mechanical connection to transfer torque, however, when the shaft is overloaded, it faces the risk of being broken, which puts the safety of the equipment at risk. Permanent magnet coupling (PMC) makes it possible to transfer the torque in a non-contact way. Moreover, when the torque is exceeded, the loading equipment can be protected by the magnetic slip [1]-[2]. The absence of mechanical wear is another benefit of PMC. The vibration that is felt on the shaft will be amplified step by step due to the mechanical connection. While in the PMC, the amplification of shaft vibration can be avoided through the non-contact connection. Therefore, the service life of the coupling can be prolonged.

Permanent magnet eddy current coupling (PMEC) is one of the PMCs that possesses all of the benefits of PMC. It consists of a primary rotating disc with a permanent magnet (PM) and a load rotating disc with a copper ring. When the primary rotating disc is propelled by a prime mover, a rotating magnetic field will be resulted from the PM and pass through the copper ring. Therefore, the corresponding eddy current will be produced in the load rotating disc, allowing for the production of the so-called armature magnetic field. Therefore, the electromagnetic torque can be generated via the interaction between the copper ring eddy current-induced magnetic field of the armature and the PM magnetic field. The copper ring and PM design determine the PMEC's performance [3]-[5].

The mechanism of a conventional disc type permanent magnet eddy current drive was first proposed by A. Wallace and C. Wohlgemuth in 1995, and thus the first PMEC has manufactured. A. Wallace also proposed the variable-speed disc type PMEC in 2001 [6]-[7]. For the PMEC, two distinct structures were developed in the past decades, including the axial flux PMEC and the radial flux PMEC [8]-[9]. The axial flux PMEC has capable of maximizing magnetic flux

† Corresponding Author : State Key Laboratory of Reliability and Intelligence of Electrical Equipment (School of Electrical Engineering, Hebei University of Technology), Tianjin 300130, China.(2016020@hebut.edu.cn)

* State Key Laboratory of Reliability and Intelligence of Electrical Equipment (School of Electrical Engineering, Hebei University of Technology), Tianjin 300130, China.(13290408919@163.com)

** State Key Laboratory of Reliability and Intelligence of Electrical Equipment (School of Electrical Engineering, Hebei University of Technology), Tianjin 300130, China.(985646120@qq.com)

*** State Key Laboratory of Reliability and Intelligence of Electrical Equipment (School of Electrical Engineering, Hebei University of Technology), Tianjin 300130, China.(wangyi@hebut.edu.cn)

**** School of Electrical and Data Engineering, University of Technology Sydney, Ultimo, NSW 2007, Australia.(gang.lei@uts.edu.au)

***** School of Electrical and Information Engineering, University of Sydney, Sydney, NSW 2006, Australia.(jianguo.zhu@sydney.edu.au)

Received 02 Feb 2023 ; Accepted 03 Mar 2023

utilization and thus the high torque ability can be achieved. The magnetic flux can be regulated by inserting a shielding layer in radial flux PMEC, therefore the speed can be regulated more straightforwardly. For the conventional PMEC, the PM is mounted on the surface of the primary rotating disc. The PM will be subjected to centrifugal force, therefore the conventional PMEC cannot be employed for high speed drive application. By installing the PM in the rotating disc, the mechanical strength of the PMEC has been improved greatly, therefore it can be employed for high speed operation.[10]. Meanwhile, for improving the performance of the PMEC, the PM designed with the Halbach array is proposed [11].

To obtain the electromagnetic performance of the PMEC, the analytical method was extensively investigated in the past. The 3D magnetic structure of the PMEC is simplified with the 2D magnetic circuit for the magnetic field calculation and performance prediction, and the combination of the analytical method and the finite element method (FEM) was proposed[12]-[16]. The eddy current loss produced in the copper ring is the main heat source of PMEC, and obtaining the accurate eddy current loss is the basis for the temperature field calculation. For computing the eddy current loss accurately, combining a 3D analytic eddy current field calculation model with the 3D FEM is an effective way [17]. The electric-magnetic-thermal coupling method was proposed for determining the stable long-term temperature of PMEC components precisely [18]-[19].

PMEC has been successfully employed in pumps, fans, conveyor belts and other motor drives in power generation, metallurgy, petrochemical, water treatment, and other industries. PMEC is mainly utilized in blower and water feeder drive systems where the speed must be variable. The manner in which a converter is used to manage the speed is heavily influenced by the surrounding environment. When driving a high-temperature or high-pressure corrosive load, converter maintenance is a challenging issue. Meanwhile, the switching loss and conduction loss of the converter reduce the energy conversion efficiency. Through experimental verification, compared with the converter, the adjustable speed PMEC has the advantages of low loss, highly reliable operation, and low vibration noise [20]. However, the performance of PMECs in speed regulation has been given little attention in the past, as conventional PMECs have some structural disadvantages. By changing the coupling depth, the speed of the traditional axial flux PMEC can be regulated, whereas by varying the shielding layer insertion depth the speed of the radial flux PMEC can be controlled. Traditional PMEC is plagued by the following issues [21]:

- Low space utilization
- Imprecise speed regulation
- Lagging speed regulation
- narrow speed regulation range
- Large installation space

In this paper, an axial-radial flux hybrid excitation permanent magnet eddy current coupling (HE-PMEC) is proposed. Both the axial and radial air gap are employed for the energy conversion, therefore, the space utilization and the performance of the proposed HE-PMEC can be enlarged when compared with the PMEC. The axial magnetic field is produced by a DC excitation current, whereas the radial magnetic field is produced by a ferrite magnet. Consequently, compared with the PMEC which is only excited by the PM, the proposed HE-PMEC can achieve superior starting and braking performance, as well as a greater capacity for speed regulation.

The structure of this paper is as follows: Section 2 explains HE-PMEC's construction and parameters. Section 3 examines the magnetic field distribution, presents the variable current starting and braking curves and speed regulation performance, and validates the temperature stability of HE-PMEC. Section 4 examines the effect of the axial pole number and radial pole number on the maximum load torque, and a new improved multilevel optimization technique is proposed to optimize the copper ring shape. In Section 5, the main performance of the proposed HE-PMEC is compared with PMECs of different structures: single radial flux (SRE), single axial flux (SAE), dual radial flux (DRE), dual axial flux (DAE), axial-radial NdFeB permanent magnet flux (ARNE), and axial-radial ferrite flux (ARFE), and HE-PMEC. The final section is the conclusion.

2. Structure of HE-PMEC

The structure of the HE-PMEC can be seen in Figure 1, and it consists of two primary electromagnetic parts: the first is the primary rotating disc, which is connected with the prime mover, and both the PM and the shielding layer are located on the primary rotating disc; the second is the load rotating disc, which is connected with the load, and it is the location of the copper ring and the side wall.

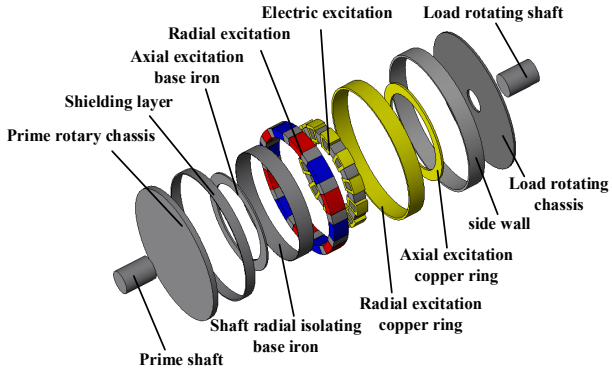

Fig. 1. Structure of HE-PMEC

The detail of the primary rotating disc and the load rotating disc are shown in Figure 2. Figure 2 (a) shows the primary rotating disc. The ferrite magnet is employed to produce the PM magnetic field in the radial air gap. Specifically, the ferrite magnets are magnetized along the radial direction and the magnetization direction of the adjacent PMs is opposite. Meanwhile, the DC winding is taken to produce the axial air gap magnetic field. Therefore, both the axial air gap and radial air gap can be employed for the electromagnetic energy conversion and both the PM and DC excitation current can be adopted for producing the magnetic field. Figure 2(b) shows the load rotating disc, which includes the radial copper ring and axial copper ring which mounted on the inner surface of the load rotating disc.

The stainless steel shielding layer can be inserted and removed between the copper ring and the PMs, which can play the role of insulating the copper ring from the magnetic field generated by the ferrite magnet. There is no eddy current resulted in the shielding layer since it rotates at the same speed as the primary rotating disc, without relative displacement.

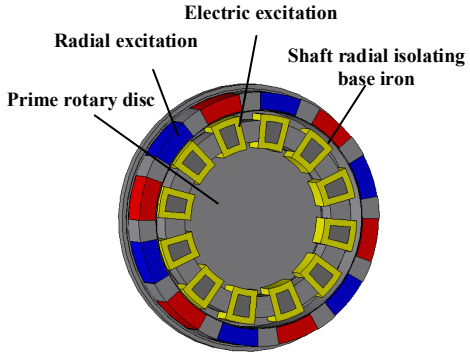

(a)

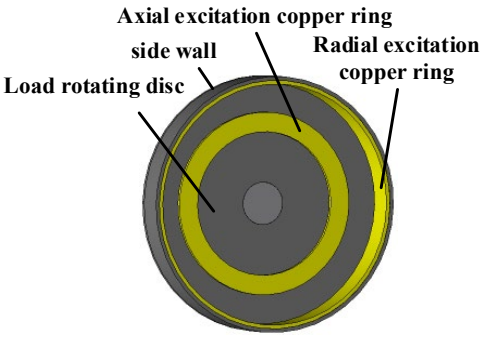

(b)

Fig. 2. (a) Primary rotating disc (b) load rotating disc

Table 1 tabulates the main parameters of HE-PMEC. The HE-PMEC proposed in this paper is applied to the blower load, for which a rated torque of around 20 Nm is required. Considering the safety of operation, the maximum torque is set at 30 Nm. Within the mechanical strength of the coupling shaft, it is possible to arbitrarily determine the rotational speed of the prime mover. In this article, 1500 rpm is used.

Table 1 Main Parameters of HE-PMEC

Parameter	Value	Unit
Prime mover speed (n_1)	1500	rpm
Rated load torque (T_L)	30	Nm
Mechanical moment of inertia (J)	0.0018	kg/m^2
Moment of inertia (GD)	0.071	N·m^2
Rated axial excitation current density (J_e)	8	A/mm^2
Maximum DC excitation current density (J_m)	20	A/mm^2
Distance between two turntables	62	mm
Length of radial magnetized PM	50	mm
Length of the DC excitation magnet core	38	mm
Coupling outer diameter	410	mm
Shaft outer diameter	70	mm
Number of poles of radial permanent magnet	12	--
The outside diameter of the radial permanent magnet	386	mm
The inner diameter of the radial permanent magnet	335	mm
The circumferential angle of radial PM	20	deg
Number of axial flux core sections	12	--
The sectional area of the axial flux coil	370	mm
The outer diameter of the axial flux core	300	mm
The inner diameter of the axial flux core	236	mm

3. Performance Analysis of HE-PME

3.1 Magnetic field analysis

For the magnetic field analysis and performance calculation, the JMAG transient electromagnetic field analysis module based on the 3D FEM is used. Figure 3 illustrates the no-load magnetic flux density distribution (no relative rotation between the primary rotating disc and the load rotating disc). As shown, the maximum magnetic flux density in the radial copper ring is around 0.27 T, while the maximum magnetic flux density in the axial copper ring is

approximately 0.43 T.

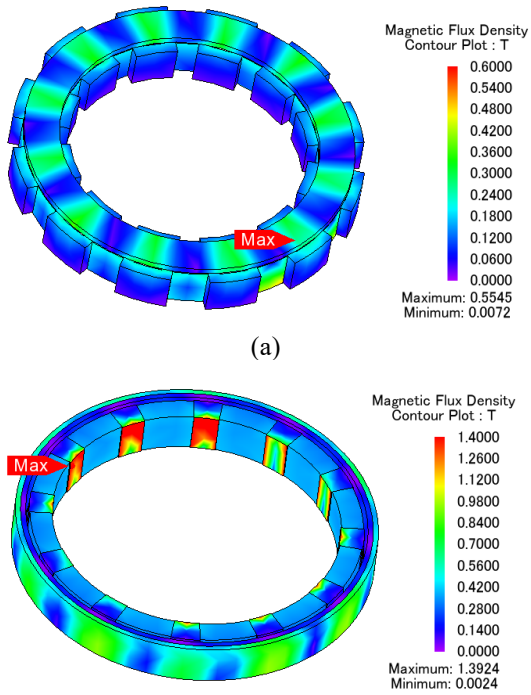

Fig. 3. No load flux density distribution (a) on the axial flux structure and (b) on the radial flux structure

Figure 4 shows the distribution of magnetic flux density on each component of HE-PMEC under the rated load condition (the loading speed is 1451 rpm, and the load is dragged for 30 Nm). The maximum magnetic flux density in the radial copper ring is around 0.34 T, while the maximum magnetic flux density in the axial copper ring is approximately 0.32 T.

Under the rated load state, the magnetic flux density on the radial copper ring and the axial copper ring is comparable, as indicated. Under load operation, the magnetic density of the axial copper ring decreases compared with that under the no-load operation, while the magnetic density of the radial copper ring increases. The eddy current in the radial copper ring strengthens the magnetic field, whereas the eddy current in the axial copper ring weakens the magnetic field.

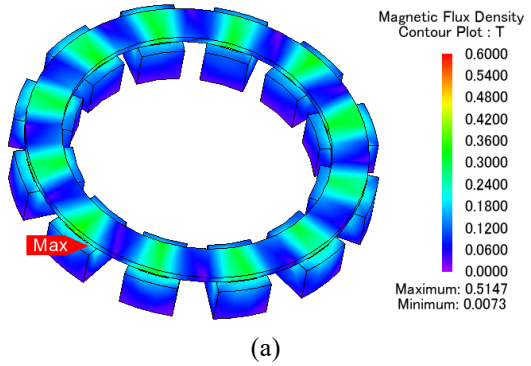

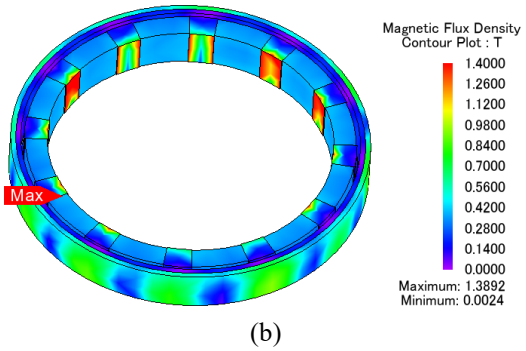

Fig. 4. Rated load flux density distribution (a)on the axial flux structure and (b)on the radial flux structure

Figure 5 illustrates the magnetic flux density distribution in the axial and radial air gaps under rated load and no load. Figure 5 (a) and (b) depict the radial air gap magnetic density distribution before and after load operation. As shown, the eddy current distributed on the radial copper ring enhances the air gap magnetic field. Figure 5 (c) and (d) depict the magnetic density distribution in the axial air gap before and after load operation, respectively. It can be seen that the eddy current resulted in the axial copper ring reduces the axial air gap magnetic field.

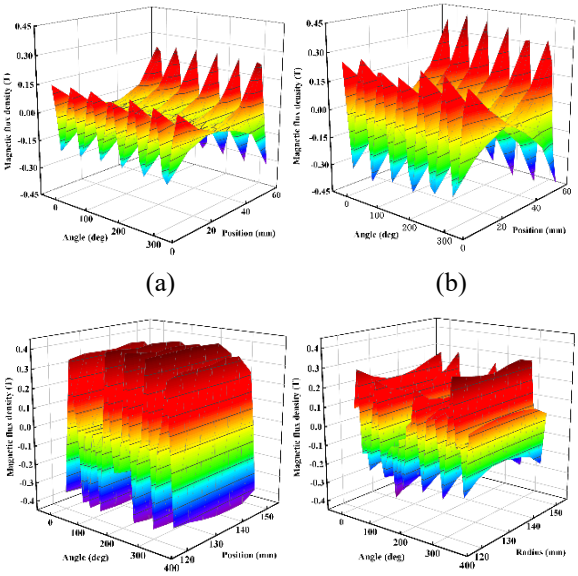

Fig. 5. (a) No load radial air gap flux density distribution, (b) rated load radial air gap flux density distribution, (c) no load axial air gap flux density distribution, and (d) rated load radial air gap flux density distribution

3.2 Starting process analysis

The starting torque can be regulated flexibly during the starting process in the HE-PMEC. The relationship between starting torque and speed is determined by,

$$J\frac{d\omega_L}{dt} = T_e - T_L - D\omega_L - K\theta_L \quad (1)$$

where, J is the mechanical moment of inertia, ωL is the mechanical angle velocity of the load shaft, θL is the mechanical angle of the load shaft, Te is the electromagnetic torque provided by the load rotating disc, TL is the load torque, D is the torque damping coefficient, K is the torsional elastic torque coefficient.

If the damping torque and torsional elastic torque are ignored, the above equation can be simplified as,

$$J\frac{d\omega_m}{dt} = T_e - T_L \quad (2)$$

According to the operating characteristics of PMEC, equation (2) can be written as,

$$\frac{GD^2}{375}\frac{dn_L}{dt} = \frac{GD^2 a_n}{375} = T_{start} - T_L \quad (3)$$

where, GD2 is the moment of inertia, n is the rotational speed of the load rotating disc, and Tstart is the starting torque of HE-PMEC.

According to equation (3), the starting process is determined by the starting torque, and the higher the starting torque, the faster the speed of the load shaft rises. The relationship between the starting torque and the force on the shaft is determined by,

$$F = ma_n = \frac{375m}{GD^2}(T_{start} - T_L) \quad (4)$$

where an is the acceleration of the load shaft.

As shown, as the starting torque increases, the force on the shaft increases as well. However, the force on the shaft may be caused to exceed the mechanical limit if the acceleration process is too fast. The maximum starting torque(MST) is related to the diameter of the shaft and the material, in this paper, we use a 24 mm diameter No.45 steel shaft, so MST is set to 191Nm.

Figure 6 illustrates the torque of the HE-PMEC at various load shaft speeds and DC winding current densities. To provide a speedy and gentle starting process, the shielding layer is not put between the PM and copper ring. As demonstrated, during the starting procedure, torque increases before decreasing. MST is approximately 97.3 Nm when the DC excitation current is around 8 A/mm2. Increasing the DC excitation current density enhances the starting torque. As load speed increases, the torque steadily declines until it reaches the rated value of 30 Nm at 1435 rpm.

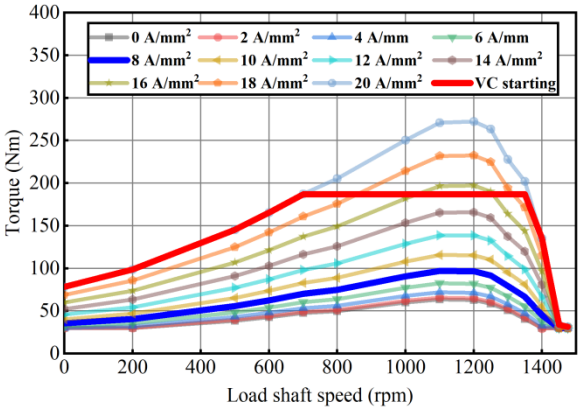

Fig. 6. Start curve of HE-PMEC

During the starting process (speed increasing from 0 to rated), the torque increases first and then decreases. The blue curve shown in Figure 6 is the starting curve with a DC excitation current density of 8 A/mm2. The red curve shows the torque versus the speed when the speed varied from 0 to 700 rpm and the DC excitation current density equals 20 A/mm2, and the torque when the speed increases from 700 to 1200 rpm and the DC excitation current density falls progressively. As illustrated in Figure 6, when the speed increases from 1200 to 1348 rpm, the DC excitation current density should be increased gradually to maintain a starting torque of 182 Nm. Maintaining a DC excitation current density of 20 A/mm2 until boosting speed to rated. Finally maintain 8 A/mm2 rated operating current

By adjusting the DC excitation current, the average torque and MST of the HE-PMEC can be increased to 179 Nm and 182 Nm, respectively, which are significantly greater than keeping a constant current of 8 A/mm2. Consequently, by using the variable current starting (VC starting) method, the HE-PMEC is with superior starting performance compared to other PMECs. The red curve is the VC starting curve.

3.3 Speed regulation process

The speed can be regulated by changing the insertion depth of the shielding layer or the DC excitation current. Figure 7 illustrates the effect of shielding layer insertion depth and DC excitation current on speed regulation. Considering that the load torque of HE-PMEC is fixed constantly. When the shielding layer is completely absent and the maximum DC excitation current density is 20 A/mm2, the maximum load speed can reach 1451 rpm. The rotational speed will decrease as the DC excitation current decreases or the insertion depth of the shielding layer increases.

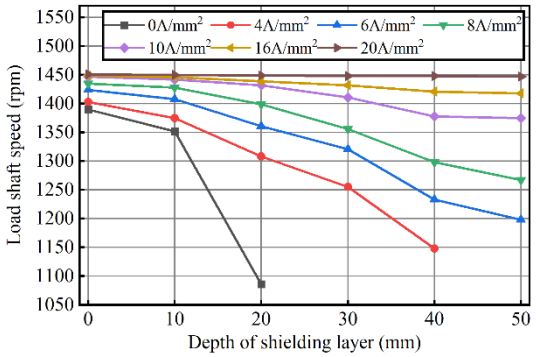

Fig. 7. Speed regulation curve of HE-PMEC

Under the rated DC excitation current density (8 A/mm2), the load shaft speed without the shielding layer inserted between the radial PM and the copper rings is approximately 1435 rpm. When the shielding layer is fully placed in between the radial PM and the copper ring, the load shaft speed can be decreased to 1267 rpm, with a speed regulation range of around 168 rpm. When the DC excitation current density is 0 A/mm2, the lowest possible speed is 1082 rpm, and the speed regulation range is around 308 rpm.

If the shielding layer's insertion depth remains unchanged, the speed can be controlled by adjusting the DC excitation current. Specifically, the load shaft speed decreases as the DC excitation current diminishes. Meanwhile, the speed regulation range expands as the insertion depth of the shielding layer grows. By adjusting the DC excitation current and the insertion depth of the shielding layer, the adjustable speed range and the speed regulation range of the HE-PMEC are 1082 rpm to 1451 rpm and 369 rpm respectively.

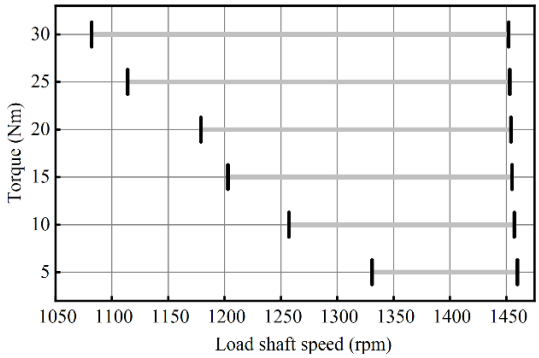

Fig. 8. Speed regulation range under different load torque

Figure 8 illustrates the variation of speed regulation range from the rated load torque of 30 Nm to the load torque of 5 Nm. As illustrated, as the load torque reduces, the maximum speed increases, however, the minimum speed also increases, and then the speed regulation range steadily decreases.

3.4 Braking process

Braking is another key function of the HE-PMEC. When the prime mover's rotor shaft is fixed, the braking torque can be produced to progressively halt the load rotor shaft. The relationship between braking torque and speed during the braking process can be expressed by,

$$\frac{GD^2}{375}\frac{dn_L}{dt} = -T_{stop} \tag{5}$$

where, Tstop is the braking torque of HE-PMEC. The relationship between the rising speed of braking torque and the decline of speed can be expressed by,

$$F = ma_n = m\frac{dn_L}{dt^2} = \frac{375m}{GD^2}T_{stop} \tag{6}$$

As starting torque, An increase in braking torque also leads to an increase in force on the rotating shaft. The maximum braking torque (MBT) is set to the same value as the MST to protect safe operation. The DC excitation current density must be regulated to provide a rapid and smooth braking action.

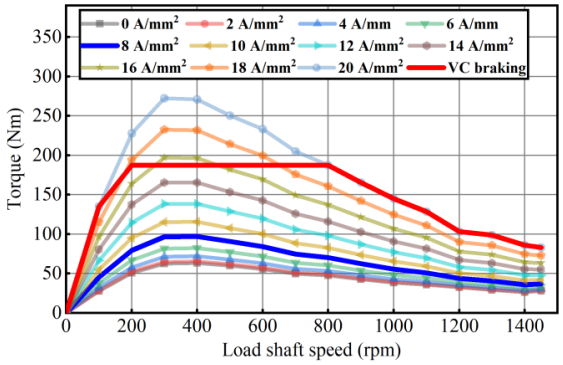

Fig. 9. Break curve of HE-PMEC

Figure 9 shows the braking curve of the HE-PMEC when the insertion depth of the shielding layer is 0 mm. As shown, the greater the DC excitation current, the greater the braking torque can be produced. The blue curve shown in Figure 9 is the braking curve when the DC excitation current equals 8 A/mm2. The red curve is the variable current breaking (VC breaking) curve with the DC excitation current varying during the braking process. When the speed is decreased from the rated speed to 900 rpm, a DC excitation current of 20 A/mm2 is utilized. When the speed is reduced from 800 rpm to 300 rpm, the DC excitation current density should gradual decreased to maintain a torque of 185 Nm. And the DC excitation current density of 8 A/mm2 should be increased gradual to maintain a torque of 185 Nm throughout the braking process from 300 rpm to 173 rpm. Finally, a DC excitation current density of 20 A/mm2 is maintained to reduce the speed to 0.

With regulating the DC excitation current, the average braking torque and torque change rate of the HE-PEMC during the braking process are 138.27 Nm and 185 Nm, respectively, which are much better than keeping a constant current of 8 A/mm2. The rate of speed reduction produced

by the rate of torque variation falls within the mechanical strength range of the shaft. Consequently, when the DC excitation current is regulated, HE-PMEC may execute the braking process speedily and stably.

3.5 Temperature field analysis

The torque provided by HE-PMEC is the result of the interaction between the magnetic field produced by the PM and DC excitation current and the magnetic field produced by the eddy currents on the copper rings. The resulting eddy currents are the primary heat sources, and the resulting significant temperature rise poses a very high demagnetization risk for the PM; hence, thermal analysis is crucial for the design and study of HE-PMEC. The computed core loss and eddy current loss serve as the basis for the thermal field analysis, and Figure 10 illustrates the coupling flowchart.

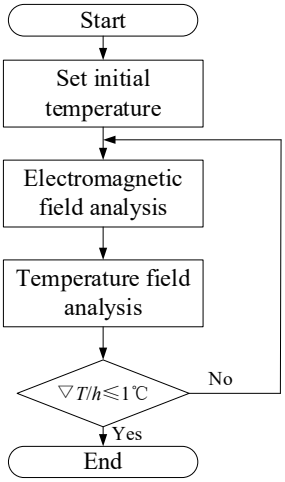

Fig. 10. Electromagnetic-temperature coupling analysis process

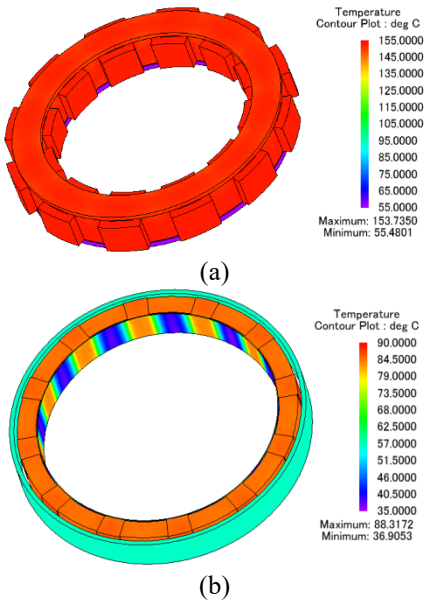

Fig. 11. (a) Temperature of axial flux part (b)Temperature of radial flux part

Table 2 Maximum Temperature of Each Part of HE-PMEC

Parts of load rotating disc	temperature（℃）	Parts of driving rotary disc	temperature（℃）
Load shaft	40.0	Prime shaft	41.0
Load rotating chassis	56.4	Prime rotating chassis	88.2
Axial rotating copper ring	55.5	Radial PM	86.7
Radial rotating copper ring	56.4	Axial flux winding	152.9
side wall	51.8	Axial flux core	153.7
Maximum temperature	56.4	Maximum temperature	153.7

Figure 11 illustrates the temperature of each component of HE-PMEC during stable long-term operation (temperature rise of no more than 1 ℃ per hour). The temperature of core compounds is shown in Table 2. As illustrated, the temperature of the axial copper ring is 55.5 ℃, the temperature of the radial copper ring is 56.4 ℃, the highest temperature of the axial flux core is 153.7 ℃, and the temperature of radial flux PM is 86.7 ℃. As the Curie temperature of the ferrite magnet is about 300 ℃, and its performance will be decreased greatly when its working temperature is over 100 ℃, the ferrite magnet worked in the proposed HE-PMEC can work safely.

4. Design and Optimization of HE-PMEC

4.1 Structural design optimization

The axial pole number (APN) and radial pole number (RPN) are critical for determining the main performance of HE-PMEC. Figure 12 illustrates the maximum load torque and PM temperature of the HE-PMEC with different APN while RPN equals 12. As shown, when RPN equals 12, the maximum load torque increases as the APN increases. However, when APN equals 14, the maximum load torque improves slightly compared to when APN equals 12, however the PM temperature increases significantly. In particular, the PM temperature of HE-PMEC with a 12/14 structure is 19.1 % higher than that of HE-PMEC with a 12/12 structure, while the maximum load torque is 3.06 % greater. Consequently, HE-PMEC with a 12/12 structure is determined for the study in this paper.

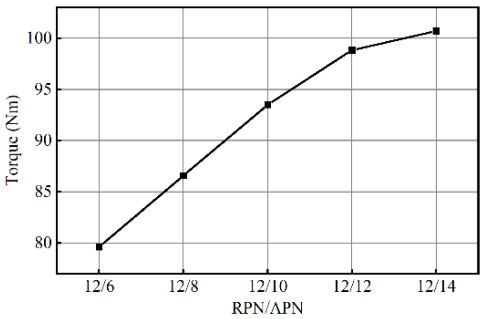

(a)

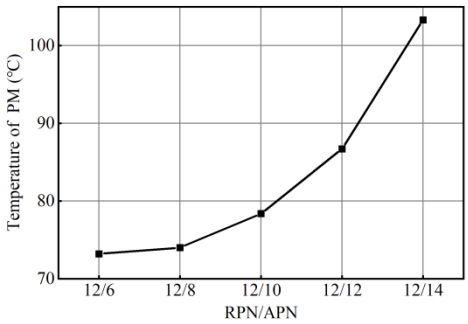

(b)

Fig. 12. (a) Maximum load torque versus the APN (b) Temperature of permanent magnet versus the APN

4.2 Optimization of HE-PMEC

The magnetic field distribution generated by the eddy current is determined by the magnetic flux density distributed on the copper ring. Therefore, it is vital to optimize the copper ring's shape in order to improve the torque performance of HE-PMEC. The magnetic flux density pattern of HE-PMEC without the shielding layer is shown in Figure 13. Since the increase in temperature will decrease the performance of the HE-PMEC, the optimization focuses on achieving a balance between the resulting eddy current and heat dissipation.

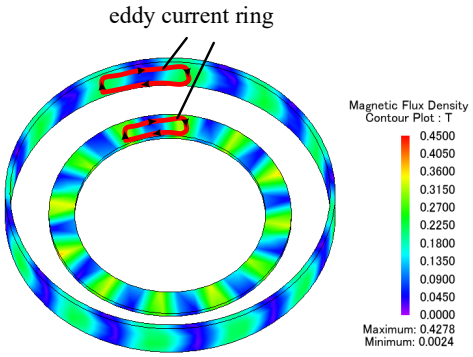

Fig. 13. Magnetic flux density on the radial and axial copper ring

As shown in Figure 13, the magnetic flux density spread on the copper rings generates an eddy current that is circularly distributed between two adjacent poles. This phenomenon is referred to as an eddy current ring. In this paper, the shape of the eddy current ring is optimized.

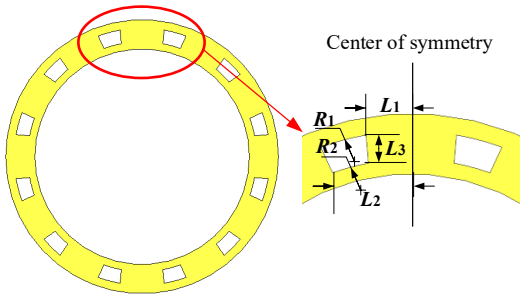

(a)

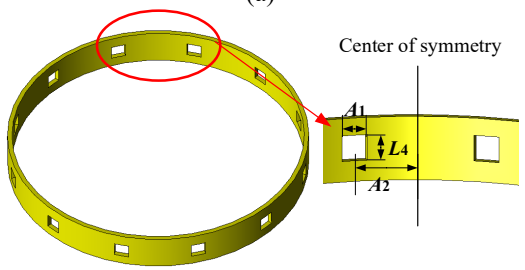

(b)

Fig. 14. Optimization parameters (a) Axial copper ring (b) Radial copper ring

The parameters for determining the copper ring forms of HE-PMEC are illustrated in Figure 14. The air ring is designed near the center of the copper ring, where the magnetic flux density and eddy current are both extremely low, and the copper ring's shape is determined by its position and the corresponding eight parameters as depicted in Figure 14. The design range of these parameters is shown in Table 3.

Table 3 Parameters of HE-PMEC

Position	Parameter	unit	Design scope
Axial copper ring	R_1	mm	130-145
	R_2	mm	115-130
	L_1	mm	10-15
	L_2	mm	40-50
	L_3	mm	12-17
Radial copper ring	A_1	deg	1-8
	L_4	mm	6-30
	A_2	deg	13-17

Copper consumption and temperature rise on PMs are chosen as optimization objectives, and DC current density, load speed, and maximum load torque as the constraints. Initially, the copper rings of the HE-PMEC do not have grooves. The optimization model is shown as follows,

$$\begin{aligned} \min \quad & F = \omega_1 \frac{W_{cu}}{W_{cu0}} + \omega_2 \frac{T_{PM}}{T_{PM0}} \\ s.t. \quad & J_c - 20 < 0 \\ & 1000 - Speed_{load} < 0 \\ & 95 - T_{max} < 0 \end{aligned} \tag{7}$$

where, Wcu and Wcu0 are copper consumption and initial copper consumption respectively, TPM and TPM0 are PM temperature rise and initial PM temperature rise respectively, Jc is the DC excitation current density, Speedload is the load speed, and Tmax is the maximum load torque.

Using intelligent optimization algorithms (such as a multi-objective genetic algorithm) for the design optimization of the above model directly is very difficult, due to there are 8 parameters need to be optimized. In order to reduce the optimization time, the multilevel optimization approach is employed. In this research, a new technique is proposed to further enhance the optimization result and efficiency of the multi-level optimization strategy. The flowchart of the enhanced new optimization technique is depicted in Figure 15.

Step 1: Generate an experiment matrix with 8 parameters based on the Hyperlatin Cube method, and construct the surrogate model based on the obtained training set from the 3D FEM calculation results, then calculate the sensitivity of these design parameters based on the constructed surrogate model.

Step 2: Divide the high-dimensional optimization problem with 8 parameters into three low-dimensional optimization problems with less than 3 parameters through sensitivity analysis.

Step 3: Optimize each low-dimensional optimization problem sequentially based on the multi-objective genetic algorithm, and the parameters with high sensitivity are optimized first.

Step 4: After optimizing all the parameters, the sensitivity of parameters are recalculated, and Step 2 and 3 will be done again.

Step 5: Repeat the optimization process until the target error of the two optimization cycles is within 1 %.

Due to the recalculation of the parameter sensitivity, the second round of optimization has a more reasonable ranking and faster convergence can be achieved compared with the traditional multilevel optimization.

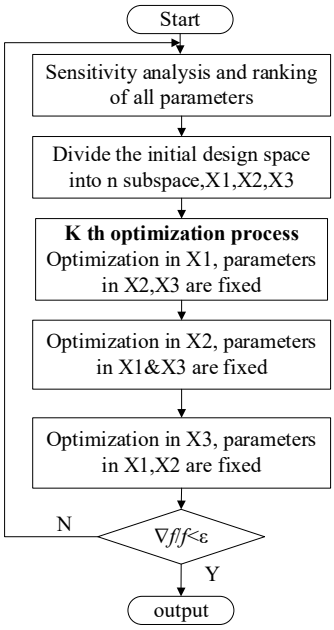

Fig. 15. Flowchart of multi-level sequential optimization strategy

Table 4 illustrates the design parameters for the various low-dimensional optimization processes. It can be seen that several design parameters are re-ranked, during the second round of optimization, while L1 and L4 continue to be the two parameters with the highest sensitivity. Table 5 tabulates the parameter values before and after each level's optimization.

Table 4 Parameters for different low dimensional optimization

Round	Level	parameter
1	1	L_1 L_4
	2	A_1 L_2 R_2
	3	L_3 A_2 R_1
2	1	L_4 A_1
	2	L_1 L_2 A_2
	3	L_3 R_2 R_1

Table 5 Value of design parameter and performance at each level

Parameter (mm)	Round					
	1			2		
	Level			Level		
	1	2	3	1	2	3
R_1	140	140	139.2	139.2	139.2	139.1
R_2	126.5	124.8	124.8	124.8	124.8	124.3
L_1	11.7	11.7	11.7	11.7	10.6	10.6
L_2	46.7	44.7	44.7	44.7	44	44
L_3	14	14	15.2	15.2	15.2	15.6
A_1	5	7.2	7.2	9.3	9.3	9.3
L_4	24.4	24.4	24.4	27.1	27.1	27.1
A_2	15	15	15.9	15.9	16.3	16.3
W_{cu} (kg)	4.66	4.48	4.37	4.34	4.33	4.33
T_{PM} (℃)	82.3	77.6	74.3	73.7	73.5	73.5

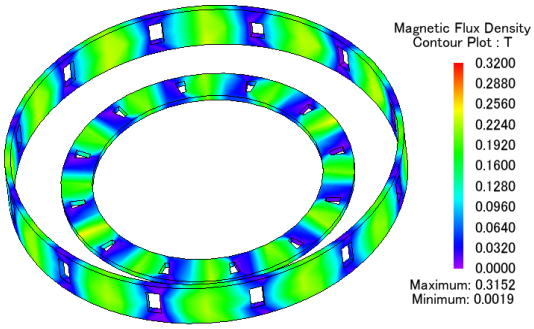

Fig. 16. Optimized magnetic density distribution of copper ring

Figure 16 illustrates the structure and the magnetic density distribution of the two copper rings of the optimized HE-PMEC. As illustrated, the magnetic flux density distribution of the optimized HE-PMEC is more concentrated. Table 6 shows the copper consumption, maximum load torque, maximum temperature of axial and radial copper rings, permanent magnet temperature, and speed regulation range of HE-PMEC before and after optimization. After optimization, the maximum temperature of the copper ring and PM decreases significantly. In the meantime, copper consumption falls from 4.81 kg to 4.33 kg. However, both the maximum load torque and the speed regulation range are slightly reduced.

Table 6 Performance comparison

	HE-PMEC (ini)	HE-PMEC (opt)
copper consumption (kg)	4.81	4.33
max load torque (Nm)	98.5	95.3
max temperature of axial copper rings(℃)	55.5	51.3
max temperature of radial copper rings(℃)	56.4	51.8
max temperature of PM(℃)	86.7	73.5
speed regulation range (rpm)	1082-1451	1090-1449

5. Comparison of PMECs with Different Structures

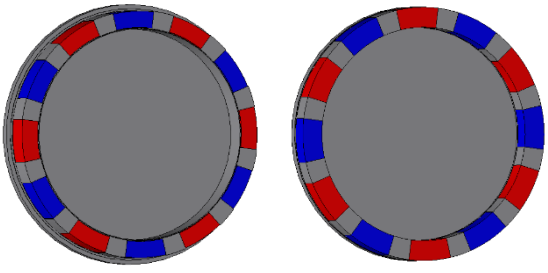

(a) (b)

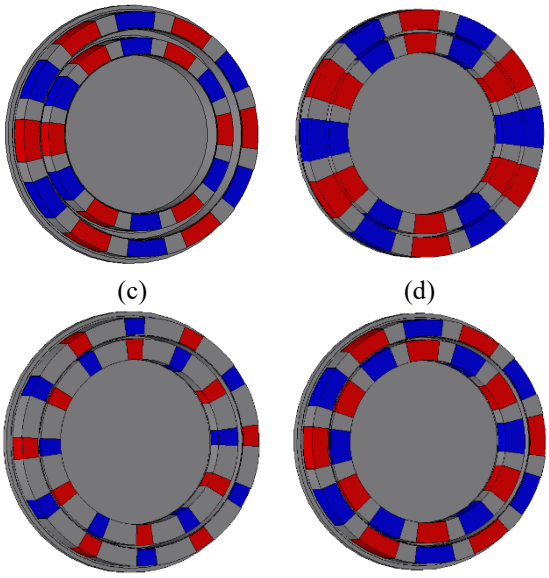

(c) (d) (e) (f)

Fig. 17. PMEC with different structures (a)SRE (b)SAE (c)DRE (d)DAE (e)ARNE (f)ARFE

Figure 17 depicts the six different structures of the prime rotating disc of PMEC. Ferrite is used to generate the magnetic field of SRE, SAE, DRE, DAE, and ARFE among these PMEC. Considering that the price of NdFeB is eight times higher than that of ferrite magnet, the amount of NdFeB consumed in ARNE is one-eighth that of ferrite magnet consumed in other PMECs. These PMECs are with the same load rotating disc structure as the HE-PMEC illustrated in Figure 2(b), the same inner and outer diameters of the prime rotating disc, the same PM volume, and the same material properties for each component.

Figure 18 shows the starting and braking curves comparison between these PMECs and HE-PMEC.

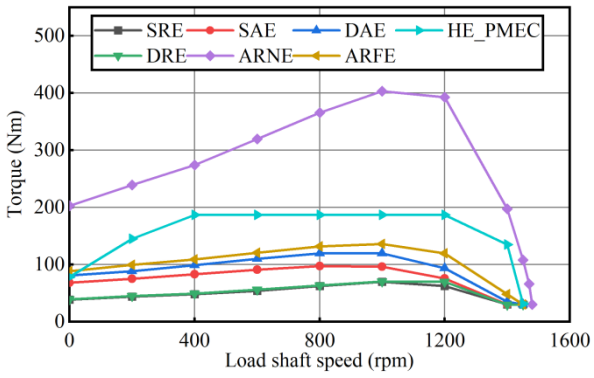

(a)

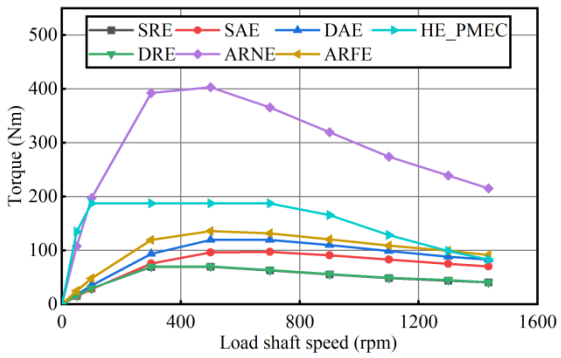

(b)

Fig. 18. (a)Starting curve comparison, (b)braking curve comparison

As shown, SRE and DRE have the lowest starting torque and braking torque, whereas DAE and SAE have greater starting torque and braking torque, respectively. Due to the high remanence of NdFeB, ARNE is able to achieve exceptionally high starting torque and braking torque; however, the torque grows rapidly. MST and MBT is 400 Nm and 403 Nm, respectively, which exceeds 191 Nm. The starting and braking processes demonstrate that the NdFeB is unsuitable for producing the magnetic field of PMEC in this case. During VC starting and VC braking process, the torque achieved by HE-PMEC is greater than that of PMECs with ferrite magnets, and MST(182 Nm) and MBT(169 Nm) is acceptable. The comparison above demonstrates HE-PMEC's superior starting and stopping capability.

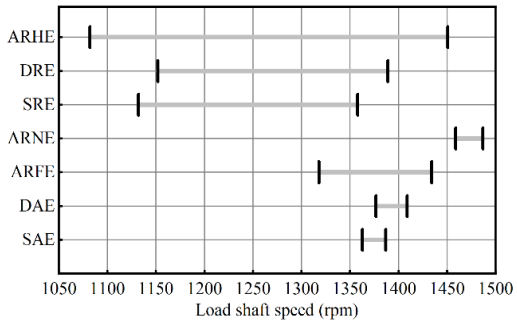

Fig. 19. Speed regulation range

The speed regulation range of these PMECs is depicted in Figure 19. As shown, the greatest speed regulation range for HE-PMEC occurs when the DC excitation current density is less than 20 A/mm2. As the insertion depth of the shielding layer can be adjusted flexibly, PMECs with radial flux structure can have excellent speed regulation performance and a broad speed regulation range. For the PMECs with axial flux structure, adjusting the air gap distance between the primary rotating disc and the load rotating disc may regulate the speed of the load shaft. However, the speed regulation range is narrow. The speed regulation range of DRE is greater than that of SRE, however, the speed regulation range of DAE and SAE are comparable. ARFE's speed regulation range is significantly greater than ARNE's. From the viewpoint of speed regulation, NdFeB is also inappropriate for the PMEC poles.

As shown, among these PMECs. ARNE has the maximum speed, and the lowest speed that can be adjusted is greater than the maximum speed of all other PMECs. HM-PMEC has the largest speed regulation range. The maximum speed that can be adjusted by HE-PMEC is only second to ARNE, and the minimum speed that can be adjusted is the smallest of all PMECs.

6. Conclusion

A HE-PMEC is proposed and analyzed in this paper. The ferrite magnet is adopted for producing the radial magnetic field and the DC excitation current is employed for producing the axial magnetic field. Moreover, the shielding layer is developed for adjusting the radial magnetic field. As the axial magnetic field is produced by the DC excitation current, therefore the starting and braking performance, and the speed regulation range of the HE-PMEC can be controlled flexibly. By comparing the calculated no load and rated load magnetic flux density in the axial and radial air gap, it can be seen that the axial air gap flux density will be reduced while the radial air gap flux density will be enhanced when the HE-PMEC is under loading. Moreover, the axial and radial air gap flux density are comparable when the HE-PMEC is under rated loading state. Through the temperature field analysis, it can be seen that the temperature rise is within the allowable range and has large design redundancy. For the design optimization, an improved multilevel design optimization is proposed, it can be seen that the heat dissipation can be increased and the temperature rise can be reduced by deleting some copper in the copper ring. Compared with other PMECs, HE-PMEC shows better starting and braking performance and more wide speed regulation range, as both the radial PM magnetic field and the axial magnetic field can be regulated.

Acknowledgements

This work was supported by the state key laboratory of reliability and intelligence of electrical equipment (school of electrical engineering, hebei university of technology) and province-ministry joint key laboratory of EFEAR.

References

[1] Ravaud R, Lemarquand G, Lemarquand V, and Depollier C (2009) Permanent magnet couplings: field and torque three-dimensional expressions based on the Colombian model. IEEE Trans Magn 45(4):1950-1958. doi:

10.1109/TMAG.2008.2010623

[2] Kang L, Jonathan Z. B (2016) A 3-D Analytical Model of a Halbach Axial Magnetic Coupling. In: 2016 International Symposium on Power Electronics, Electrical Drives, Automation and Motion, jeju, 2016, pp 1448-1454. doi: 10.1109/SPEEDAM.2016.7525881

[3] Mohammadimmai S, Mirsalim M (2014) Design Optimization of Double-sided Permanent magnet Radial-flux Eddy-current Couplers. Electric Power Systems Research 108(2014):282-292. doi: 10.1016/j.epsr.2013.11.014

[4] Wang R, Furlani E (2013) Design and Analysis of Axial Permanent Magnet Coupling Based on 3D FEM. IEEE Trans Magn 30(4): 2292-2295. doi: 10.1109/TMAG.2013.2243129

[5] Thierry L, Smail M, and Abderrezak R (2012) Simple Analytical Expressions for the Force and Torque of Axial Magnetic Couplings. IEEE Trans Energy Convers 27(2):536-546. doi: 10.1109/TEC.2012.2183372

[6] Wallace A, Wohlgemuth C (1999) Seamless pump manufacture at maximum velocity. World Pumps 1999(394):33,35-36. doi: 10.1016/S0262-1762(99)91080-5

[7] Wallace A, Jouanne A, Jeffreys R (2000) Comparison Testing of an Adjustable-Speed Permanent Magnet Coupling. IEEE IAS 80(11): 277-282. doi: 10.1109/PAPCON.2000.854194

[8] Kang L, Jonathan Z. B, Vedanadam M. A. (2017) Ideal Radial Permanent Magnet Coupling Torque Density Analysis. IEEE Trans Magn 53(6): 1-4. doi: 10.1109/TMAG.2017.2668139

[9] Julien F, Thierry L. Denis N (2016) Axial-field Eddy-current coupling: a 3D test problem for numerical experiments. Int J Numer Model EL. 2018; 31: e2217. doi: 10.1002/jnm.2217

[10] Mohammadi S, Mirsalim M, Vaez-Zadeh S, Talebi H (2014) Design Analysis of a New Axial-Flux Interior Permanent-Magnet Coupler. In: The 5th Power Electronics, Drive Systems and Technologies Conference (PEDSTC 2014), jeju, 2014, pp 562-567. doi: 10.1109/PEDSTC.2014.6799437

[11] Jang G, Kim J, Shin H, Choi JY (2017) Optimal design and torque analysis considering eddy-current reduction of axial-flux permanent magnet couplings with Halbach array based on 3D-FEM. In: Electromagnetic Field Computation, jeju, 2017, pp 1. doi: 10.1109/CEFC.2016.7816179

[12] Thierry L, Abderrezak R (2015) Steady-State and Transient Performance of Axial-Field Eddy-Current Coupling, Analytical Modeling and Analysis of Axial Flux Interior Permanent Magnet Couplers. IEEE Trans Ind Elec 62(1): 2287-2296. doi: 10.1109/TIE.2014.2351785

[13] Li Z, Zhang L, Qu B, Yang H, Wang D (2021). Evaluation and analysis of novel flux-adjustable permanent magnet eddy current couplings with multiple rotors. IET Electric Power Applications, 15(6): 754-768. doi: 10.1049/elp2.12072

[14] Yang X, Liu Y, Wang L (2019) Nonlinear Modeling of Transmission Performance for Permanent Magnet Eddy Current Coupler. Mathematical Problems in Engineering, 2019, 2019(10):1-14. doi: 10.1155/2019/2098725

[15] Chen M (2021). General 3d analytical method for eddy-current coupling with halbach magnet arrays based on magnetic scalar potential and h-functions. Energies, 14(24): 8458. doi: 10.3390/en14248458

[16] Jian W, Lin H, Fang S, Huang Y (2014) A General Analytical Model of Permanent Magnet Eddy Current Couplings. IEEE Trans Magn 50(1), 1-9. doi: 10.1109/TMAG.2013.2279073

[17] Xu W, Dazhi W (2011) Calculation of Eddy Current Loss and Thermal Analysis for Adjustable Permanent Magnetic Coupler.In: 2011 International Conference on Electronic & Mechanical Engineering and Information Technology jeju, 2011:1-4. doi: 10.1109/EMEIT.2011.6024012

[18] Zheng D, Wang D, Li S, Shi T, Li Z, Yu L (2017) Eddy current loss calculation and thermal analysis of axial-flux permanent magnet couplers. AIP Advances 7, 025117 (2017). doi: 10.1063/1.4977702

[19] Cheng X, Liu W, Luo W, Sun M, Zhang Y (2022). A simple modelling on transmission torque of eddy-current axial magnetic couplings considering thermal effect. IET Electric Power Applications, 16(4): 434-446. doi: 10.1049/elp2.12165

[20] Wallace A, Jouanne A, Jeffreys R (2001) Performance Testing of Power Electronic and Permanent-Magnet Adjustable-Speed Drives. Electric Power Components and Systems, 2001(29):1123–1132. doi: 10.1080/153250001753246853

[21] Amged S, El-Wakeel (2014) Design optimization of PM coupling using hybrid particle swarm optimization simplex method(PSO-SM) algorithm. Electric Power Systems Research, 2014, 116: 29-35. doi: 10.1016/j.epsr.2014.05.003

Hongming Zhang
He received the B.E. degree in electrical engineering from Hebei University of Technology, Tianjin China, in 2021. His research interests include the electromagnetic device design optimization method and strategy.

Chengcheng Liu
He received the B.E. degree and in automation from Yangzhou University, Yangzhou, China, in 20107. He received the PH.D degree in electrical engineering from Hebei University of Technology, Tianjin, China, in 2015. His research interests include the design, analysis, and control of machines.

Shiwei Zhang
He received the B.E. degree in electrical engineering from Jilin Institute of Chemical Technology, Jilin, China, in 2019. His research interests include the design, analysis, control and optimization of electromagnetic devices.

Youhua Wang
He received his B.S., M.S. and Ph.D. degrees in electrical engineering from Xi'an Jiaotong University, Hebei University of Technology and Fuzhou University in 1987, 1990 and 1994, respectively. His research interests include integrated effects of engineering electromagnetic fields.

Gang Lei
He received the B.S. degree in Mathematics from Huanggang Normal University, China, in 2003, the M.S. degree in Mathematics and Ph.D. degree in Electrical Engineering from Huazhong University of Science and Technology, China, in 2006 and 2009, respectively. His research interests include computational electromagnetics, design optimization and control of electrical drive systems and renewable energy systems.

Jianguo Zhu
He received the B.E. degree in 1982 from Jiangsu Institute of Technology, Jiangsu, China, the M.E. degree in 1987 from Shanghai University of Technology, Shanghai, China, and the Ph.D. degree in 1995 from the University of Technology Sydney (UTS), Sydney, Australia, all in electrical engineering. His research interests include computational electromagnetics, measurement and modelling of magnetic properties of materials, electrical machines and drives, power electronics, renewable energy systems and smart micro grids.